J Nanopart Res (2017) 19: 124
DOI 10.1007/s11051-017-3818-6

RESEARCH PAPER

Synthesis of carbon-doped nanosheets m-$BiVO_4$ with three-dimensional (3D) hierarchical structure by one-step hydrothermal method and evaluation of their high visible-light photocatalytic property

Deqiang Zhao · Wenjuan Zong · Zihong Fan · Yue-Wen Fang · Shimin Xiong · Mao Du · Tianhui Wu · Fangying Ji · Xuan Xu

Received: 24 October 2016 / Accepted: 5 March 2017 / Published online: 24 March 2017

Abstract To achieve an efficient visible-light absorption and degradation of bismuth vanadate ($BiVO_4$), in this paper, a carbon-doped (C-doped) nanosheets monoclinic $BiVO_4$ (m-$BiVO_4$), with thicknesses within 19.86 ± 8.48 nm, was synthesized using polyvinylpyrrolidone K-30 (PVP) as a template and L-carbonic as the carbon source by one-step hydrothermal synthesis method. This C-doped $BiVO_4$ in three-dimensional (3D) hierarchical structure enjoys high visible-light photocatalytic property. The samples were characterized using x-ray diffraction, scanning electron microscope, Raman spectra, energy dispersive spectrometer, transmission electron microscope, x-ray photoelectron spectroscopy, UV–Vis diffused reflectance spectroscopy, specific surface area, electron spin resonance, and transient photocurrent response, photoluminescence spectra, and incident-photon-to-current conversion efficiency, respectively. What is more, we studied the C-doping effect on the band-gap energy of $BiVO_4$ based on First-principles. X-ray diffraction analysis showed that all photocatalysts were in the same single monoclinic scheelite structure. According to the other characterization results, the element C was successfully doped in $BiVO_4$, resulting in the 3D hierarchical structure of C-doped $BiVO_4$ (P-L-$BiVO_4$). We speculated that it could be the directional coalescence mechanism by which the L-cysteine promoted the two-dimensional growth and C-doping process of $BiVO_4$, thus leading to the formation of nanosheets which were then promoted into 3D self-assembly by PVP and the shortening of the band gap. Among all samples, P-L-$BiVO_4$ can make the highest removal ratio of rhodamine B under visible-light irradiation. The stability of P-L-$BiVO_4$ was verified by recycle experiments. It showed that P-L-$BiVO_4$ had strong visible-light absorption behavior and high electron–hole separation efficiency and stability, making a significant advantage in actual situation.

D. Zhao · W. Zong · S. Xiong · M. Du · T. Wu · F. Ji · X. Xu
Key Laboratory of Three Gorges Reservoir Region's Eco-Environment Ministry of Education and National Centre for International Research of Low-carbon and Green Buildings, Chongqing University, Chongqing 400067, China

D. Zhao · W. Zong · S. Xiong · M. Du · T. Wu · F. Ji (✉) · X. Xu (✉)
National Centre for International Research of Low-Carbon and Green Buildings, Chongqing University, No. 174 Shazhengjie, Shapingba, Chongqing 400045, China
e-mail: jfy@cqu.edu.cn
e-mail: xuxuan@cqu.edu.cn

Z. Fan
School of Environmental and Biological Engineering Chongqing Technology and Business University, Chongqing 400067, China

Y.-W. Fang
Key Laboratory of Polar Materials and Devices, Ministry of Education, Department of Electronic Engineering, East China Normal University, Shanghai 200241, China

Y.-W. Fang
Nanostructures Research Laboratory, Japan Fine Ceramics Center, Nagoya 456-8587, Japan

Keywords Visible-light photocatalytic property · Carbon doping · Nanosheets · Bismuth vanadate ($BiVO_4$) · Environmental applications · Three-dimensional (3D) hierarchical structure

Introduction

In recent years, bismuth compounds have attracted extensive concerns as a preferred photochemical catalyst in the visible range. Bismuth compounds mainly include bismuth oxide (Yan et al. 2014), halogen-free bismuth oxide (Zhang et al. 2008b), bismuth sulfide (Manna et al. 2014), bismuth vanadate ($BiVO_4$) (Kudo et al. 1998), bismuth tungstate (Natarajan et al. 2014), carbonate bismuth oxide (Allured et al. 2014), bismuth titanate (Allured et al. 2014), and so on. Due to Bi 6s orbital and O 2p orbital hybridization, the semiconductor oxide has a small band-gap energy and shows great potential in the photochemical and photocatalytic field (Wang et al. 2014a). Among compounds such as bismuth oxyhalide (Br, Cl, and I) (Natarajan et al. 2016), Bi_2O_3 (Azman et al. 2016), Bi_2S_3 (Uddin et al. 2016), and $Bi_2O_2(CO_3)$ (Chang et al. 2016), $BiVO_4$ is an inexpensive, stable, and non-toxic ternary compound semiconductor, with direct semiconductor band gap of about 2.4 eV and strong visible-light absorption capacity. However, pure $BiVO_4$ is subjected to two disadvantages, of which one is the low absorption of incident light and the other is its non-porous structure. To eliminate the first disadvantage, researchers have made attempts to modify $BiVO_4$ in the hope of improving its photocatalytic absorption efficiency and of inhibiting the recombination of electron carriers. Major modification methods include metal ion modification (Xu et al. 2008; Zhang and Zhang 2010), non-metallic particle modification (Tang et al. 2013; Yin et al. 2013), and semiconductor composite modification (Tang et al. 2013; Yin et al. 2013). Among these modification methods, metal ion modification is less recommended due to the higher cost of precious metal deposit, toxicity of some metals, inactivation of some catalysts, as well as the thermal instability of the load of metals serving as the center for electron–hole recombination. Therefore, this modification method can only improve photocatalytic activity in a very narrow range of load metal ions. As non-metallic ions can enter into a semiconductor and replace oxygen, resulting in stable chemical bonds with metal ions, the technique of non-metal ion doping has attracted worldwide attention. By doping such non-metallic ions as F, C, N, and S, the band structure of $BiVO_4$ can be adjusted, thereby improving its photocatalytic properties (Geng et al. 2014; Huang et al. 2015). In response to the second disadvantage, it is mainly needed to improve the structure, morphology, and particle size of $BiVO_4$, so as to make great improvement of its photocatalytic performance (Libor Kvítek et al. 2008; Wang et al. 2014a). Among all polymorphs of $BiVO_4$, only monoclinic $BiVO_4$ (m-$BiVO_4$) has a band gap of 2.4 eV, allowing it to have visible absorption capacity (Strobel et al. 2008; Yu et al. 2009; Zhang et al. 2009a, b). Structure, morphology, and particle size are greatly influenced by the preparation methods and conditions. So far, the preparation methods of $BiVO_4$ include solid-phase method, hydrothermal synthesis method, solvent co-precipitation method, micro-emulsion method, ultrasonic-assisted method, microwave-assisted method, metal-organic deposition, flame spraying method, etc. (Geng et al. 2014; Lim et al. 1998; Tang et al. 2013; Yin et al. 2013; Zhang and Zhang 2010). Conventional law of solid-phase synthesis (Lim et al. 1998) requires higher temperature and longer reaction duration, but results in large particles and small surface area, which are not conducive to the absorption of the incident light or to the improvement of photocatalytic activity. Although the traditional co-precipitation method is simple, it may lead to poor purity and uncontrollable morphology and size of the product. In recent years, the hydrothermal synthesis of $BiVO_4$ photocatalyst has attracted increasing attention for its simple operation process, easiness in structure control, and good morphology of materials. Through adjusting the synthesis conditions such as pH value, temperature, reaction time, and the type of structure-directing agent, we can prepare $BiVO_4$ in different morphologies and structures, such as particle-like $BiVO_4$, spindle body-like $BiVO_4$, tube-like $BiVO_4$, leaf-like $BiVO_4$, line-like $BiVO_4$, nanoblock $BiVO_4$, ellipsoid body $BiVO_4$, star-like $BiVO_4$, etc. Good morphology can improve the catalyst's activity as well as absorption capacity of light (Kho et al. 2011; Liu et al. 2010; Su et al. 2009; Sun et al. 2009; Wang et al. 2011; Wei et al. 2010; Xi and Ye 2010). A lot of researches have been conducted to overcome the disadvantages of $BiVO_4$. Nevertheless, few reports have looked into morphology control via carbon doping (C-doping) of non-metallic doping. In this paper, a carbon-doped three-dimensional (3D) hierarchical nanosheet $BiVO_4$ was synthesized using a

simple hydrothermal method, in the hope of overcoming both disadvantages in a simple one-step way.

In this paper, by using PVP as structure-directing agents and L-cysteine as carbon sources, a flower-like 3D C-doped m-$BiVO_4$ with strong capacity of visible-light absorption was synthesized by one-step hydrothermal method. Using rhodamine B (RhB) as the simulated organic pollutant, the photocatalytic properties of C-doped 3D hierarchical $BiVO_4$ were investigated, finding that the C-doped 3D m-$BiVO_4$ made a better performance in catalyzing and degrading the simulated pollutant under visible-light irradiation as compared with the pure $BiVO_4$ and the two-dimensional (2D) C-doped $BiVO_4$ nanosheet structure. Further, we speculated the possible mechanism that may lead to crystal growth and photocatalytic performance enhancement, which may be due to the mechanism that the L-cysteine promoted the 2D growth of $BiVO_4$ and C-doping process, while PVP promoted 2D $BiVO_4$ nanosheets into 3D self-assembly according to contrast test and density functional theory (DFT). Carbon doping can reduce the band gap of $BiVO_4$ and thus improve the absorption of visible light, while 3D hierarchical structure can enhance the separation of electrons and holes. The C-coped flower-like $BiVO_4$ with 3D structure synthesized by one-step hydrothermal synthesis method is expected to be further applied and modified in practice.

Experimental

Experimental materials

In this experiment, we used analytically pure chemicals such as bismuth nitrate ($Bi(NO_3)_3{\cdot}5H_2O$; Chengdu Area of the Industrial Development Zone Xinde Mulan, China), sodium hydroxide powder (NaOH; Chongqing Chuandong Chemical Company, China), polyvinylpyrrolidone K-30 (PVP) in analytical grade (Chengdu Kelong Chemical Co. Ltd. China), L-cysteine (Aladdin Industrial Corporation), ammonium metavanadate (NH_4VO_3; Chongqing Chuandong Chemical Company, China), nitric acid (HNO_3; Chengdu Area of the Industrial Development Zone Xinde Mulan, China), rhodamine B (RhB; Tianjin Guangfu Fine Chemical Research Institute, China), and ethylene glycol (Chongqing Chuandong Chemical Company, China).

Catalyst preparation

Synthesis of pure $BiVO_4$

To synthesize pure $BiVO_4$, 2 mmol $Bi(NO_3){\cdot}5H_2O$ was dissolved in 4 mL of 4 mol/L HNO_3 and 50 mL of deionized water, and then subjected to constant stirring for 30 min before resulting in solution called solution A. On the other hand, 2 mmol NH_4VO_3 was dissolved in 4 mL of 2 mol/L NaOH and subjected to 30 min of constant stirring, resulting in solution B. After that, solution A and B were mixed together and then transferred into 100 mL of Teflon-lined autoclave to be sealed and heated at 180 °C for 16 h. Subsequently, the system was naturally cooled down to room temperature. The final product was collected from the mixture system by centrifuging treatment, washed with distilled water and ethanol six times, and dried under vacuum overnight at 60 °C for 12 h.

Synthesis of PVP-assisted $BiVO_4$ (P-$BiVO_4$)

To synthesize PVP-assisted $BiVO_4$ (P-$BiVO_4$), 2 mL of 0.5% PVP was added into solution A, while the remaining procedures were the same as those for synthesizing pure $BiVO_4$.

Synthesis of C-doped $BiVO_4$ (L-$BiVO_4$)

To synthesize C-doped $BiVO_4$ (L-$BiVO_4$), 0.6 mmol L-cysteine was added into solution A, while the remaining procedures were the same as those for synthesizing pure $BiVO_4$.

Synthesis of C-doped 3D hierarchical $BiVO_4$ (P-L-$BiVO_4$)

To synthesize C-doped 3D hierarchical $BiVO_4$ (P-L-$BiVO_4$), 2 mL of 0.5% PVP and 0.6 mmol L-cysteine were added into solution A, while the remaining procedures were the same as those for synthesizing pure $BiVO_4$, resulting in a sample called P-L-$BiVO_4$.

Characterization

The crystal structures of all prepared samples were characterized by x-ray diffraction (XRD) using a Rigaku D/Max2500pc diffractometer under Cu K radiation. The scanning angle of 2θ ranged from 10 to 70°, and the

scanning rate was set as 4°/min. Scanning electron microscopy (SEM) images were obtained using a Tescan FEG-SEM microscope (high voltage = 10 kV; TESCAN, MARI3, Czech Republic). Transmission electron microscopy (TEM) was conducted using JEM-3010 (JEOL, Japan) at an acceleration voltage of 300 kV. The photoluminescence (PL) spectra of the photocatalysts were obtained using a Hitachi F-7000 spectrometer with an excitation wavelength of 280 nm. Energy dispersive spectrometer (EDS) was carried out during the SEM measurements. Raman spectra were obtained using an HR evolution instrument under an Ar+ laser source of 532 nm. The surface chemical environments were analyzed according to x-ray photoelectron spectra (XPS) on a PHI5000 Versa Probe system with monochromatic Al K x-rays. UV-Vis diffuse-reflectance spectroscopy (UV-Vis DRS) was performed using a Hitachi U-3010 UV-Vis spectrophotometer. Through mixing samples in a 50 mM DMPO solution tank (aqueous dispersion for DMPO-•OH and methanol dispersion for DMPO-$\bullet O_2^-$), we prepared the samples for electron spin resonance (ESR) measurement. In this experiment, the sample was under the irradiation of visible light. Photoelectrochemical properties of samples were evaluated using a CHI Electrochemical Workstation (CHI 760E; Shanghai Chenhua Co. Ltd., China). All experiments were performed at room temperature.

First-principles study

Band structure calculations were performed using the First-principles theory based on density functional theory with projector-augmented wave approach (Blöchl 1994). The energy cutoff was 450 eV. A Hubbard U value of 2.7 eV (Zhao et al. 2016) was applied to d orbitals of V for accurate description of the electronic properties of $BiVO_4$. An 8810 Monkhorst-Pack mesh was sampled on the Brillouin zone. The exchange correlation functional was treated within generalized gradient approximation with Perdew–Burke–Ernzerh parameterization (Zhang et al. 2008b). Energy convergence criterion of 10^{-6} eV was ensured in all calculations. The treatment of the doped system of interest was based on the virtual crystal approximation (Bellaiche and

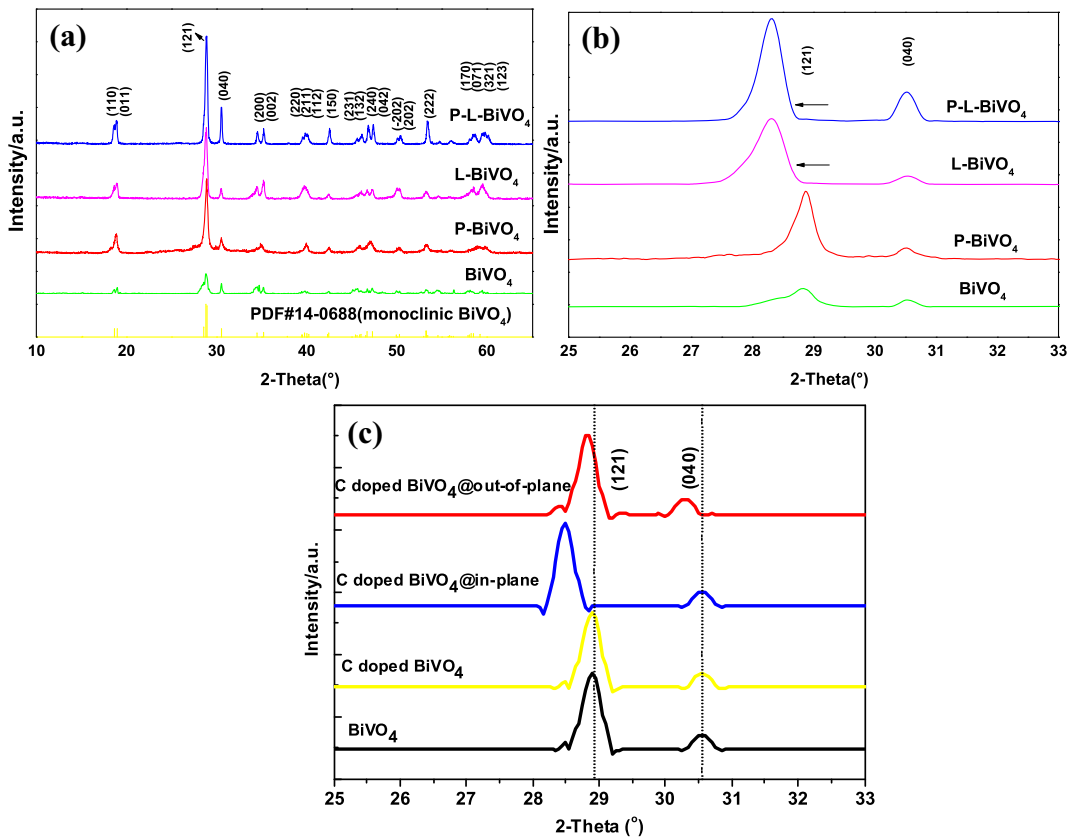

Fig. 1 **a** XRD patterns. **b** Magnified peaks of (121) and (040) planes. **c** Simulated XRD patterns of $BiVO_4$ and carbon-doped $BiVO_4$

Vanderbilt 2000). The calculated model of monoclinic $BiVO_4$ was fixed at the experimental structure. In the doped system, we considered the substitutional C at O sites in $BiVO_4$, i.e., $BiV(O_{1-x}C_x)_4$, $x = 0.01$ and 0.05.

Photocatalytic activity

The photocatalytic activities of the samples were assessed by evaluating the photodegradation degree of

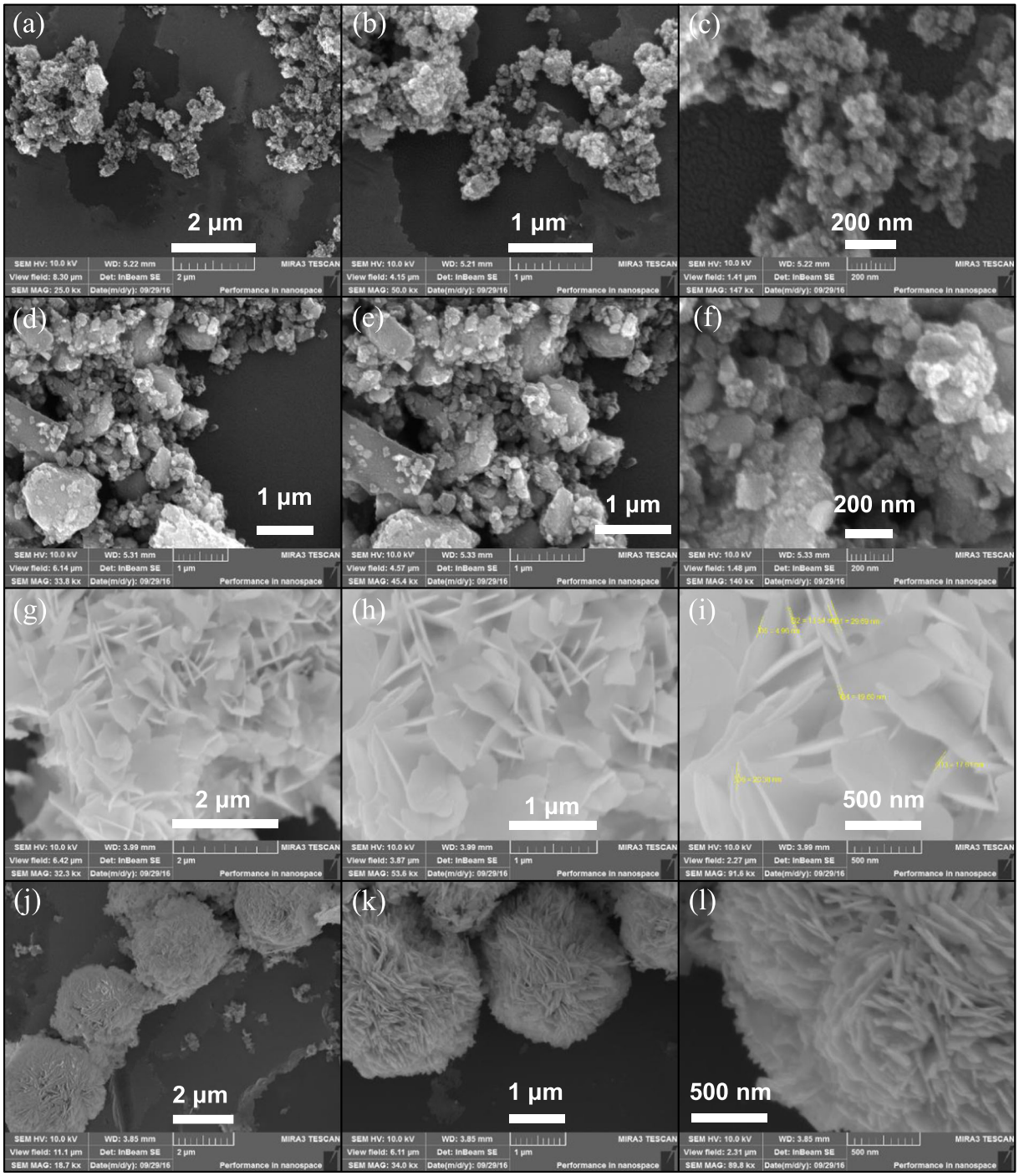

Fig. 2 SEM images of $BiVO_4$ (**a**–**c**), P-$BiVO_4$ (**d**–**f**), L-$BiVO_4$ (**g**–**i**), and P-L-$BiVO_4$ (**j**–**l**)

RhB solution under visible-light irradiation at room temperature. In the experiment, 0.20 g of catalyst was first added to 200 mL of 5 mg/L RhB aqueous solution in a 250-mL beaker and then subjected to magnetic stirring for 30 min in the dark, reaching good dispersion and adsorption–desorption equilibrium between dye and catalyst. After that, the experimental solution was placed 350 mm away from a 500-W Xe lamp with a >400 nm UV cutoff filter as the visible light irradiation source. For every 1 h of irradiation, the solution was collected and then subjected to centrifugation at 10,000 rpm to remove all catalysts. After that, the concentration of the remaining dye was spectrophotometrically monitored by measuring the absorbance of the solutions at 552 nm. For comparison, the photocatalytic experiments were carried out with pure $BiVO_4$, P-$BiVO_4$, L-$BiVO_4$, or P-L-$BiVO_4$ or no catalyst under the same conditions.

Results and discussion

Pattern and morphology analysis by XRD and SEM

Figure 1a shows the XRD spectra of the prepared samples, from which we can see all the crystal planes and related 2θ values are consistent with m-$BiVO_4$ standard powder diffraction card #PDF14-0688. According to the magnified peaks of the (121) and (040) planes in Fig. 1b, we can find that the characteristic diffraction peaks of (121) of L-$BiVO_4$ and P-L-$BiVO_4$ have smaller angle shifts than pure $BiVO_4$ and P-$BiVO_4$ after the addition of L-cysteine, which indicates that the spacing between crystal planes has become greater. This is probably due to the carbon atoms with relatively larger atomic radius (0.077 nm) that replace oxygen atoms with relatively smaller atomic radius (0.074 nm) in the $BiVO_4$ (Jagadale et al. 2008). XRD results indicate that carbon has been well inserted into the $BiVO_4$ lattice, which avoids the formation of any segregated impurity phase. As the implementation of non-metallic ion doping changes the band-gap energy, the photocatalytic activity of the sample becomes higher (Li et al. 2013; Wang et al. 2014b; Zhao et al. 2013). Therefore, the as-prepared L-$BiVO_4$ and P-L-$BiVO_4$ samples are expected to show enhanced photocatalytic performances.

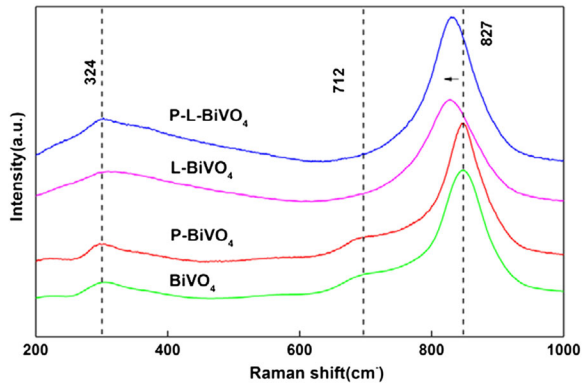

Fig. 4 Raman spectra of the samples

To explore the reason for the occurrence of a relative peak shift of C-doped $BiVO_4$, XRD patterns have been modeled by considering carbon doping and volume expansion. Considering the change of volume, we

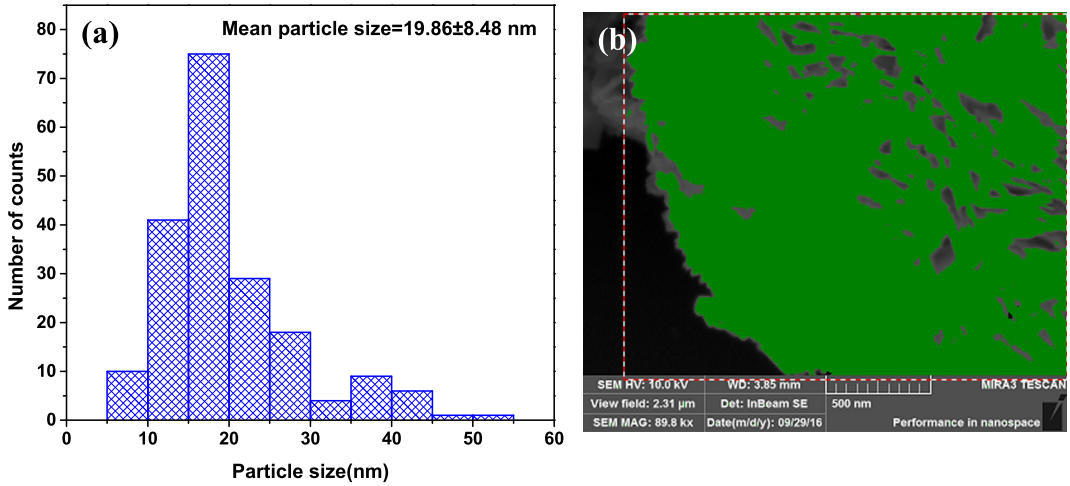

Fig. 3 **a** Particle size distribution of P-L-$BiVO_4$ obtained by measuring the thickness of 194 particles shown in SEM (**b**) images

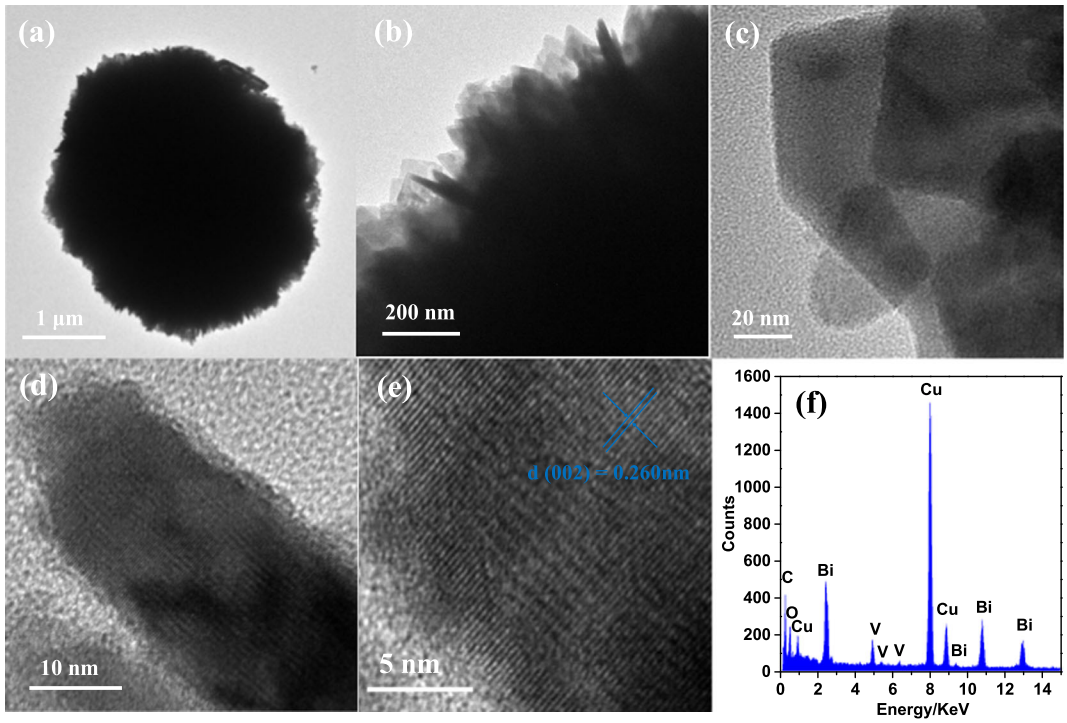

Fig. 5 HRTEM (**a**–**e**) and EDS (**f**) of P-L-$BiVO_4$

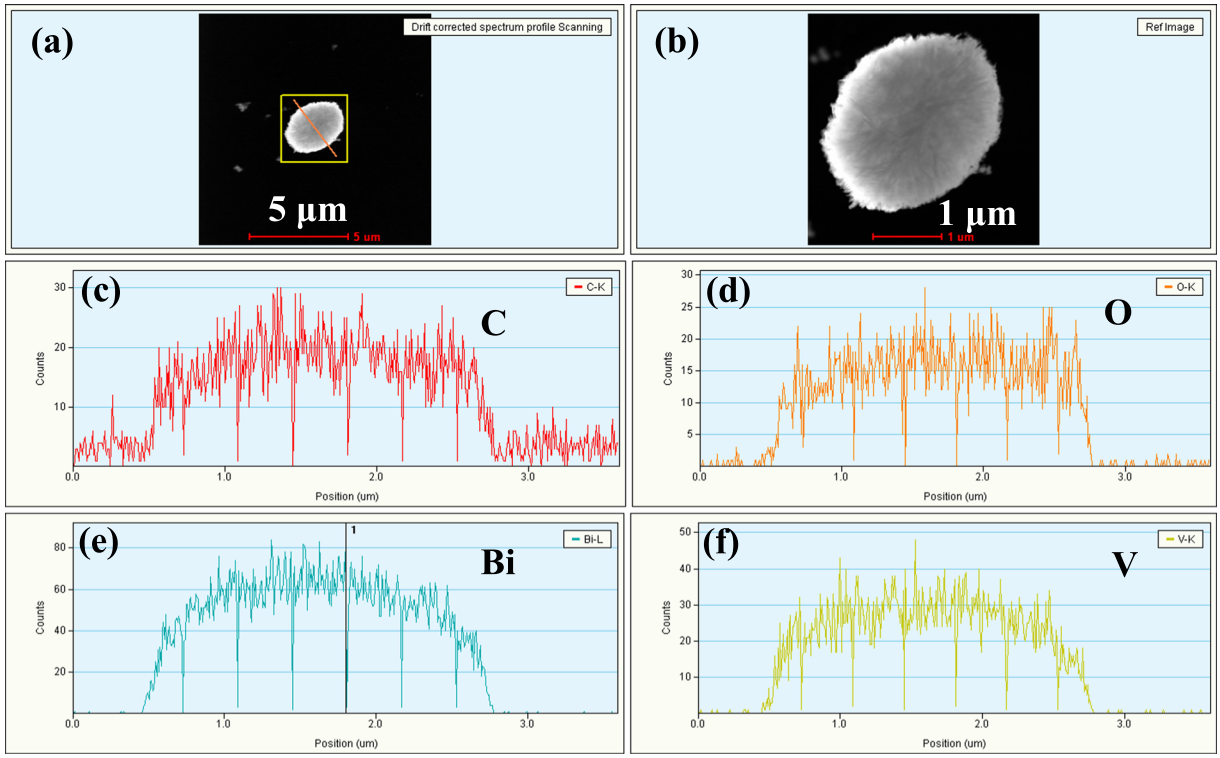

Fig. 6 EDS line scan of P-L-$BiVO_4$

simulated three cases for carbon-doped $BiVO_4$, i.e., C-doped $BiVO_4$ (including doping but not including volume expansion), C-doped $BiVO_4$@in-plane (including doping and volume expansion along in-plane direction), and C-doped $BiVO_4$@out-of-plane (including doping and volume expansion along out-of-plane direction). The simulated XRD patterns are shown in Fig. 1c, from which it can be found that the XRD pattern of C-doped $BiVO_4$ that only contains carbon dopants does not introduce any peak shift as compared with pure $BiVO_4$. However, the volume expansion along in-plane direction (C-doped $BiVO_4$@in-plane) shifts the peak (121) significantly. In the case of C-doped $BiVO_4$@out-of-plane, both peak (121) and peak (040) are shifted. By comparing the simulated XRD patterns with the experimental XRD patterns in Fig. 1b, we can conclude that the only one obvious shift (i.e., peak 121) is caused by the increase of in-plane lattice constants of carbon-doped $BiVO_4$.

Figure 2 shows the SEM of the samples. Under the condition where no structure-directing agent or carbon sources are added, the $BiVO_4$ are particles with diameters ranging from about 40 to 100 nm, in a large degree of agglomeration (see Fig. 2a–c). However, under the condition where structure-directing agent PVP is added, most of the products grew into much more bigger particles with a particle size of about 1 μm (see Fig. 2d–f). Under the condition where only carbon source L-cysteine is added, morphologies of samples are greatly changed as shown in Fig. 2g–i. The aggregations of a massive amount of nanosheets are in thicknesses ranging within 17.63 ± 8.17 nm (see D1–D6 in Fig. 2i). Under the condition where both structure-directing agent PVP and carbon sources L-cysteine are added, the morphologies of the products are changed into spherical structure, with the ball's diameter of about 2 μm. Many of these ball-shaped objects are 2D nanosheets, which are connected together, resulting in a multilayer structure like a flower (see Fig. 2j–l). The thicknesses of the composite sheets were varying within 19.86 ± 8.48 nm (194 statistical samples in Fig. 3). In conclusion, with the change of the reaction conditions, the crystal morphology of bismuth vanadate is changed accordingly. L-Cysteine contributes to its 2D growth and C-doping process, which is beneficial for electrons to migrate onto the surface and helps $BiVO_4$ to improve the range of visible light (Zhang et al. 2006), while PVP is promoting the 3D hierarchical sheet-assembled

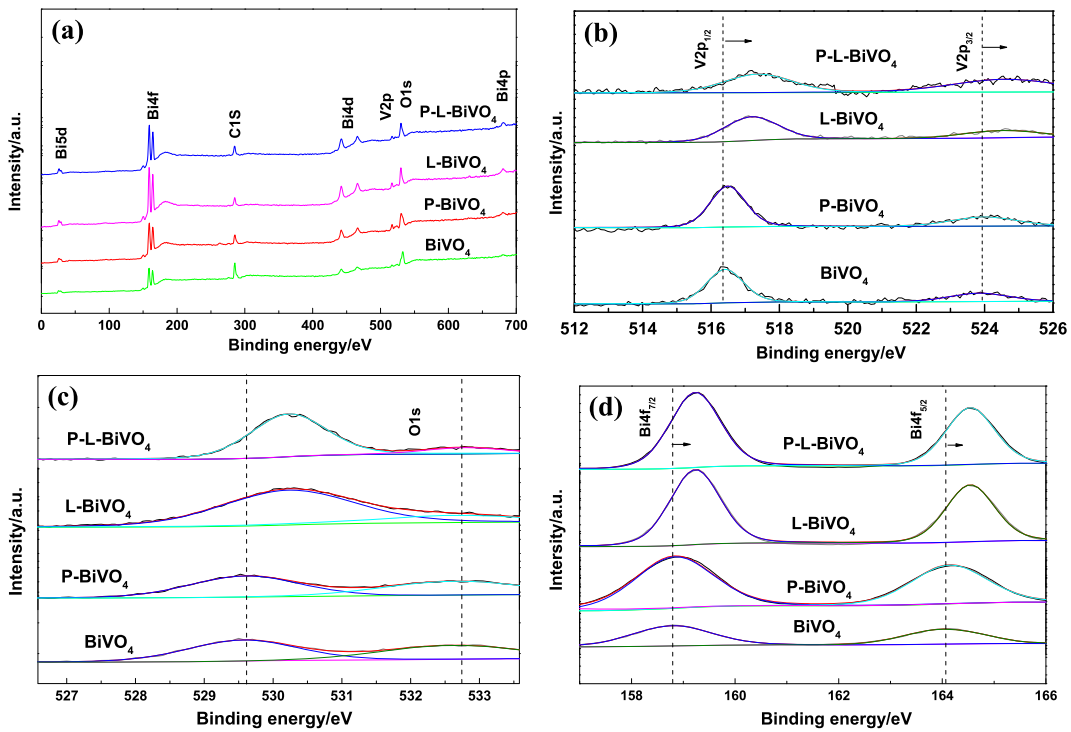

Fig. 7 X-ray photoelectron spectra of the samples: **a** survey XPS spectrum, **b** V $2_{p3/2}$ and V $2_{p1/2}$ peaks, **c** O1s peak, and **d** Bi4f5/2 and Bi4f7/2 peaks

flower-like structure. This kind of structure is reported to have reflecting and scattering effects, which is conducive to the increase of the absorption capacity of light (Xiong et al. 2014) and the enhancement of contact with contaminants (Huang et al. 2011).

Composition and chemical states analysis through Raman scattering spectra, EDS, TEM, and XPS

The peaks of Raman spectrum are sensitive to the influence of short-range ordered structure of the photocatalyst (Zhang et al. 2008a). Raman spectrum can reflect certain material information such as crystallinity, local structure, and electronic properties (Liu et al. 2003). As shown in Fig. 4, the peaks at 827, 712, and 324 cm^{-1} are ascribed to the typical vibrations of m-$BiVO_4$. The peak on 324 cm^{-1} is due to the asymmetric stretching vibration and bending vibration of VO_4^{3-}. The Raman peaks at 712 and 827 cm^{-1} can be attributed to two V–O stretching vibration modes in different orders. In addition, we can observe that the characteristic peak at 712 cm^{-1} is weak, which may be because the samples were prepared by the hydrothermal method (Galembeck and Alves 2000). On the other hand, Raman features might also be affected by sample shape. The absence of band at 712 cm^{-1} (added L-cysteine) in the Raman spectra of $BiVO_4$ thin films might be due to its low thickness (Yin et al. 2013). Owing to the addition of L-cysteine, the peak at 827 cm^{-1} is allowed to have a certain blue shift, which means the V–O band becomes longer. The blue shift is caused by the C-doping effect, i.e., carbon is inserted into the O sites of the $BiVO_4$ lattice to form the V–C bond. The V–C bond has a longer length than the V–O bond (Huang et al. 2015).

The test results of HRTEM and EDS are shown in Fig. 5. We can see that C element has been successfully doped in $BiVO_4$ and no second-phase crystal face occurs, which is consistent with XRD test results. However, the interplanar spacing of C-doped $BiVO_4$ is larger than that of PDF standard card, which indicates that the lattice constant of $BiVO_4$ has been changed due to C doping. This is mainly because as the doping C replaces the position of O, the charge imbalance occurs, thus leading to lattice distortion (Cui et al. 2010). Figure 6 shows the EDS line scan of P-L-$BiVO_4$, from which we can see that the contents of C, O, Bi, and V are higher in the middle while lower at both ends due to the 3D spherical structure of the sample.

Moreover, XPS analysis was conducted to further reveal the chemical states of samples. Figure 7a shows the fully scanned spectra in the range of 0–700 eV, and the survey spectrum shows that the composite is composed of elements Bi, O, V, and C. According to Fig. 7b, the peaks at binding energies of 523.9 (V $2p_{1/2}$) and 516.4 eV (V $2p_{3/2}$) corresponded to the split signal of V 2p while the V 2p peak is assigned to V^{5+} (Li et al. 2015). As can be seen in Fig. 7c, the samples show XPS signals of O1s at 529.7 and 532.7 eV, respectively, which is probably due to the O_2^- anions in the $BiVO_4$ crystallites. Figure 7d shows that the binding energies for Bi $4f_{7/2}$ and Bi $4f_{5/2}$ are 158.8 and 164.1 eV, respectively, which is significantly related to the Bi^{3+} peak in the monoclinic $BiVO_4$ (Kudo et al. 1999). The peak shifts of elements such as Bi, V, and O are probably due to element C that is inserted into the O sites of the $BiVO_4$ lattice, leading to the formation of C-doped

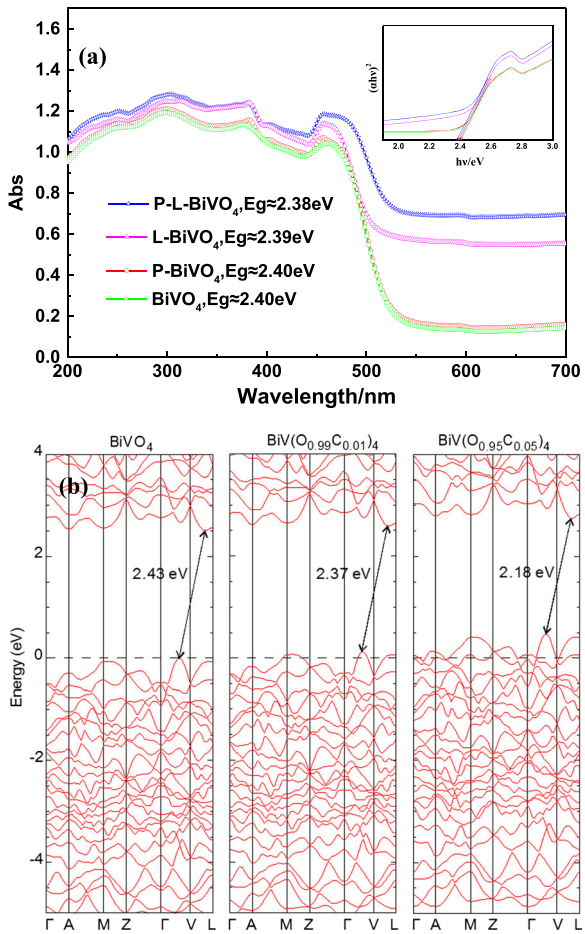

Fig. 8 **a** Estimated band gaps of UV-Vis spectra of the samples. **b** Band structures of $BiVO_4$, $BiV(O_{0.99}C_{0.01})_4$, and $BiV(O_{0.95}C_{0.05})_4$

$BiVO_4$ in the L-cysteine, which is consistent with the XRD, EDS, and Raman results.

Measurement of optical properties by UV-Vis DRS, DFT, ESR and transient photocurrent response, PL spectra, and IPCE

The UV-Vis diffuse reflectance spectra of samples are shown in Fig. 8a, from which we can see that L-$BiVO_4$ and P-L-$BiVO_4$ not only have strong absorption capacities in the ultraviolet region but also have one in the visible region. Their UV absorption capacities can be attributed to the band transition from O 2p to V 3d, while the process of visible-light absorption can be regarded as the transition from valence band (generated by hybrid orbitals of Bi^{3+} 6 s2 and O 2p) to V 3d conduction band (Xie et al. 2006). A step-shaped absorption spectrum indicates that the migration of electronics from band gap is not an impure state migration (Xiong et al. 2014). According to the UV-visible diffuse reflectance spectra, the photo energies of samples are respectively estimated as 2.4, 2.4, 2.39, and 2.38 eV according to the intercept of the tangents to plot depicting $(Ah\upsilon)^2$ versus hυ (see the inset of Fig. 8a). Therefore, the semiconductor is expected to be used as a photocatalyst under visible-light irradiation for wastewater treatment. Moreover, P-$BiVO_4$ and P-L-$BiVO_4$ have a much smaller band gap compared with pure $BiVO_4$, P-$BiVO_4$, which is mainly due to that C-doping decreases the energy of the band gap. The reason why P-L-$BiVO_4$ has stronger absorption of visible light than L-$BiVO_4$ might be due to that more C atoms enter in P-L-$BiVO_4$ (see the DFT calculation) and the 3D hierarchical structure of P-L-$BiVO_4$ has reflecting and scattering effects in some degree, thus increasing the response range and absorption capacity of light (Payne et al. 2011).

As is known to all, the DFT calculation can calculate the structure of the band gap. In this work, we conducted the DFT calculation to prove that the band gap was changed due to the C-doping. Figure 8b shows the band structures of $BiVO_4$, $BiV(O_{0.99}C_{0.01})_4$, and $BiV(O_{0.95}C_{0.05})_4$. The band structure of monoclinic $BiVO_4$ without doping is an indirect band-gap semiconductor with a wide band gap of 2.43 eV, which agrees well with the experimental band gap of 2.4 eV of pure $BiVO_4$ (Zhang et al. 2010). As for the doped systems, the band gaps of $BiV(O_{0.99}C_{0.01})_4$

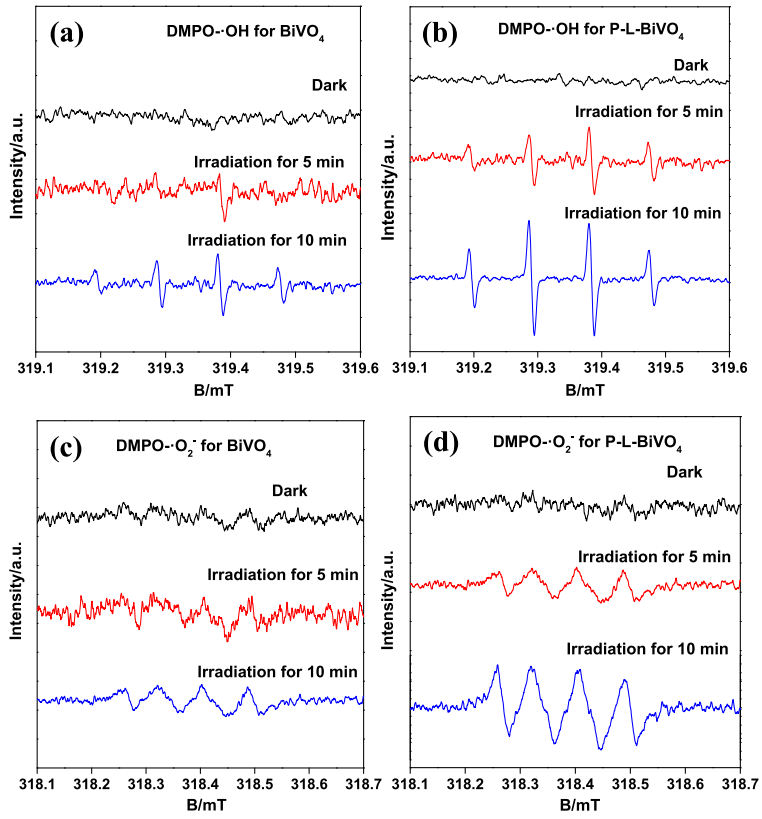

Fig. 9 DMPO spin-trapping ESR spectra under visible light: **a** DMPO-·OH for $BiVO_4$, **b** DMPO-·OH for P-L-$BiVO_4$, **c** DMPO-$\cdot O_2^-$ for $BiVO_4$, **d** DMPO-$\cdot O_2^-$ for P-L-$BiVO_4$

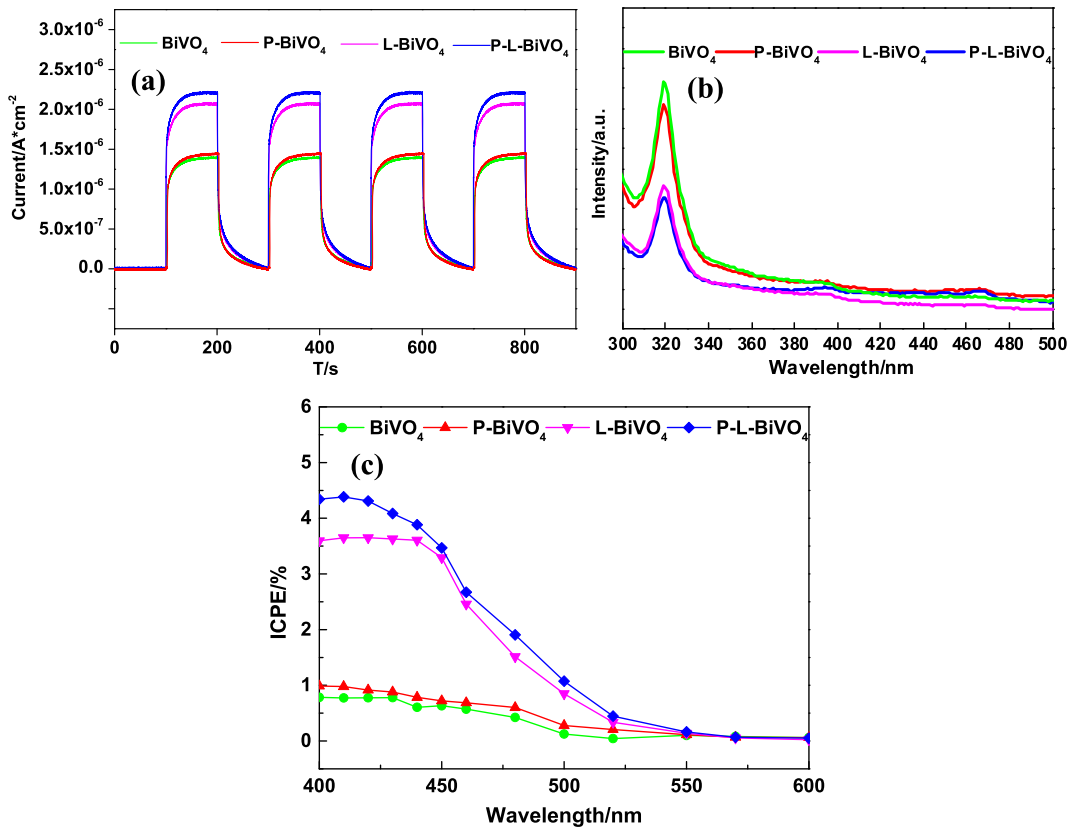

Fig. 10 **a** Transient photocurrent response. **b** PL spectra at room temperature. **c** IPCE

and $BiV(O_{0.95}C_{0.05})_4$ are estimated to be 2.37 and 2.18 eV, respectively. This suggests the substitutional C at the O sites can narrow the band gap, which is consistent with the results of our experiments.

In this research, electron spin resonance spectroscopy was adopted to detect the active radicals produced during the catalytic reaction. 5,5-Dimethyl-1-pyrroline-*N*-oxide (DMPO) was used to capture the •OH (DMPO-•OH) and $•O_2^-$ (DMPO-$•O_2^-$) generated in the catalytic process. According to Fig. 9, it can be observed that the $•O_2^-$ and $•OH^-$ signal peaks appear after 10 min of visible-light irradiation. However, there are no signal peaks of the $•O_2^-$ and •OH under dark condition. The experiment results show that the •OH and $•O_2^-$ are generated under light irradiation (Xiong et al. 2014). The signals of P-L-$BiVO_4$ appearing after 10 min of

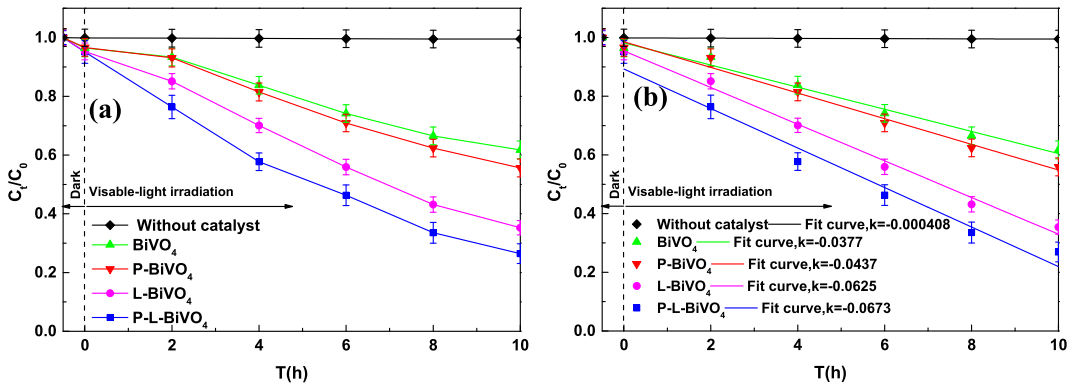

Fig. 11 **a** Degradation of RhB using different catalysts under visible-light irradiation. **b** Photocatalytic reaction with linear fitting modes and the reaction rate constant *k*

visible-light irradiation is the strongest, while that of $BiVO_4$ is significantly weaker. This indicates that the production of active species is further enhanced by the photogenerated carriers produced due to C-doping process and good morphology.

Photoelectrochemical test is usually conducted to study the excitation, separation, and transfer of carriers in a catalyst. Figure 10a shows the transient photocurrent responses of the samples under visible-light irradiation. The photocurrent densities of the P-L-$BiVO_4$ and L-$BiVO_4$ are much higher than those of $BiVO_4$ and P-$BiVO_4$, which might be attributed to C-doping process that leads to the increased usage efficiency of visible light. The photocurrent density of P-L-$BiVO_4$ is higher than that of L-$BiVO_4$, which is mainly due to that more C atoms enter in P-L-$BiVO_4$ (see the DFT calculation) and the 3D hierarchical structure of P-L-$BiVO_4$ has reflecting and scattering effects in some degree, thus leading to the increase of response range and absorption capacity of light (Hu et al. 2015). Therefore, P-L-$BiVO_4$ is expected to show excellent photocatalytic activity under visible-light irradiation.

PL spectrum is determined by the migration, transfer, and separation efficiency of the photogenerated charge carriers in semiconducting materials. PL study could effectively testify the improvement of the migration efficiency of photogenerated electrons and suppressing the recombination of electron–hole pairs. Figure 10b shows the comparisons of PL spectra of $BiVO_4$, P-$BiVO_4$, L-$BiVO_4$, and P-L-$BiVO_4$ under the excitation wavelength of 380 nm, from which we can see that the PL peak intensity of P-L-$BiVO_4$ shows a significant decreasing trend. These results show that P-L-$BiVO_4$ is conducive to the effective separation of electron–hole pair.

We have conducted an incident photon-to-current conversion efficiency (IPCE) test. The electrodes were prepared according to the method proposed by Iwase and Kudo (2010). Photoelectrochemical properties were evaluated with a three-phase electrode consisting of the working electrode (prepared electrode), counter electrode (Pt electrode), and reference electrode (saturated Ag/AgCl electrode), respectively. The working electrode was irradiated from the FTO side with visible-light through a cutoff filter. The IPCE was calculated as follows:

$$\mathrm{IPCE}/\% = (1240 \times I_{sc})/(\lambda \times P_{in})$$

where λ (nm) is the incident photon wavelength, I_{sc} ($\mu A/cm^2$) is the photocurrent of the device, and P_{in} (W/m^2) is the incident power. As shown in Fig. 10c, the monochromatic light can be obtained by grating control at 1.5 V bias voltage under Ag/AgCl condition. The IPCE of P-L-$BiVO_4$ electrode can reach 4.38% at 1.5 V versus under Ag/AgCl condition, while that of $BiVO_4$ is only 0.78% (at 410 nm). The enhancement of photoconversion efficiency indicates that P-L-$BiVO_4$ may have the best photocatalytic activity.

Table 1 Characteristics obtained from nitrogen desorption isotherms

Sample	Mean pore size (nm)	Pore volume (cm^3/g)	Surface area (m^2/g)
$BiVO_4$	17.531	0.027	4.201
P-$BiVO_4$	19.573	0.024	3.518
L-$BiVO_4$	42.132	0.071	14.351
P-L-$BiVO_4$	37.124	0.068	16.432

Evaluation of photocatalytic activity through degradation of RhB

Figure 11 shows the photocatalytic activities of the samples under visible-light irradiation for 10 h. For comparison, the self-degradation of RhB was also estimated without any catalyst. Results showed that only about 0.45% of RhB was decomposed after 10 h of irradiation without any photocatalyst, while 73.56, 64.75, 44.38, and 38.26% were degraded with P-L-$BiVO_4$, L-$BiVO_4$, P-$BiVO_4$, and $BiVO_4$, respectively. P-L-$BiVO_4$ achieved the highest catalytic activity, successively followed by L-$BiVO_4$, P-$BiVO_4$, and pure $BiVO_4$. This is mainly due to that P-L-$BiVO_4$ and L-$BiVO_4$ have relatively larger BET surface area and pore

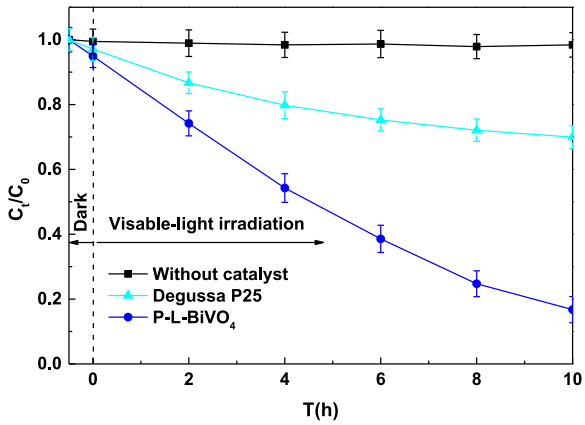

Fig. 12 Photocatalytic degradation of RhB by the as-prepared P-L-$BiVO_4$ catalyst and Degussa P25 under visible light

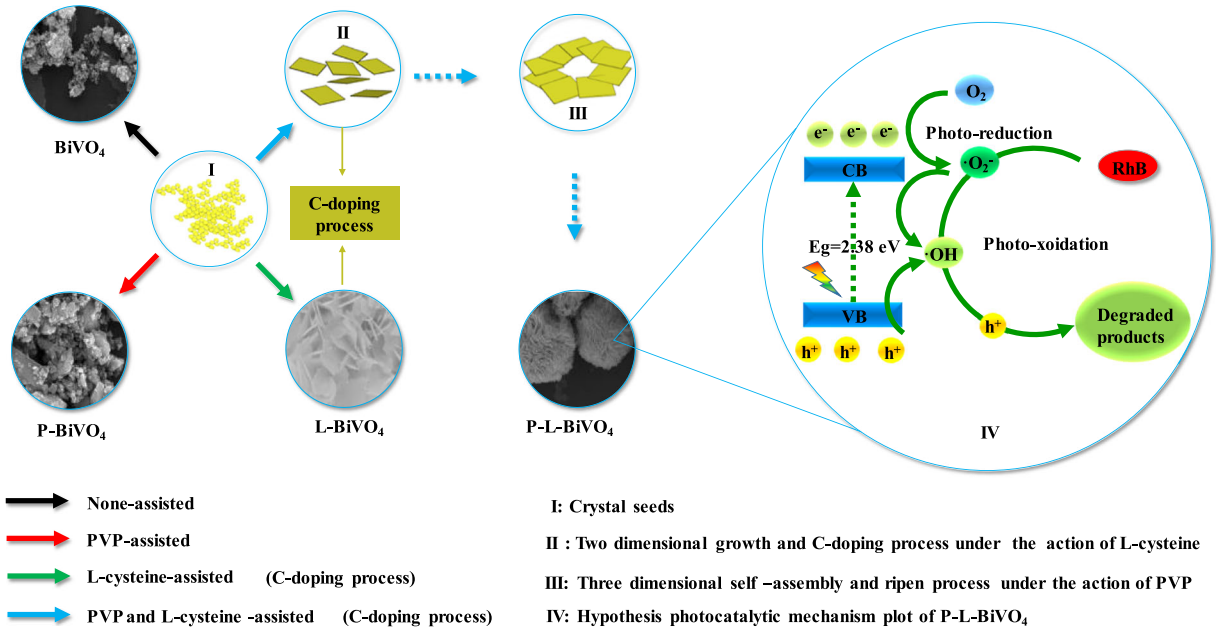

Fig. 13 Possible growth mechanism and degradation mechanism of the P-L-$BiVO_4$

volume (Table 1), which is conducive to enhancing the contact between samples and organic contaminants, so that the photocatalytic performance of samples can be improved after C-doping. On the other hand, the degradation rate of RhB is largely determined by the visible-light adsorption capacity. The band gap of $BiVO_4$ was shortened by C-doping; therefore, $BiVO_4$ enjoyed a stronger and broader absorption in the visible region. All these reasons explain why $BiVO_4$ had an increased absorption of visible light and why the degradation rate of RhB was increased.

For comparison, the photodegradation of RhB was performed using photocatalyst Degussa P25 under visible light. The results are shown in Fig. 12. Blank test showed that no RhB was degraded under visible light in the absence of photocatalyst. The as-prepared P-L-$BiVO_4$ exhibited better photocatalytic activity than Degussa P25 in the degradation of RhB under the same experimental conditions, which could degrade 83.24 and 30.05% of RhB in 10 h, respectively.

Postulated formation and degradation mechanism of photocatalysts

In the hydrothermal synthesis process of solid material, the morphology of the product is affected by various factors such as structure-directing agent, alkaline source, nature of the metal precursor, the precursor solution pH,

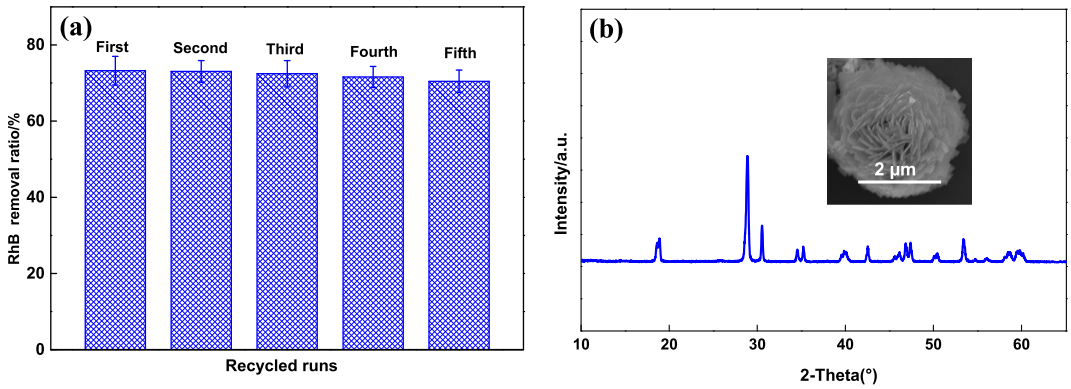

Fig. 14 **a** Cycling runs of photocatalytic degradation of RhB using photocatalyst P-L-$BiVO_4$; **b** SEM image and XRD patterns of P-L-$BiVO_4$ after five rounds of cycling

temperature, and hydrothermal time (Grassmann and Löbmann 2003; Wang et al. 2006; Xu et al. 2006; Yu and Golfen 2004). Directional coalescence mechanism can successfully account for the formation of specific crystal morphology (And and Yu 2007; Gong et al. 2006). In this mechanism, a highly ordered superstructure can be formed by the directional self-assembly of primary particles. In this paper, the $BiVO_4$ particles of various morphologies were formed by following the mechanism shown in Fig. 13. The surface energy of the nanocrystals of $BiVO_4$ could be reduced by adding L-cysteine, which was then absorbed on the surface of the nanoparticles of newly generated $BiVO_4$. L-Cysteine molecules were selectively adsorbed on the surface of the $BiVO_4$ particle (Xie et al. 2013). Due to the adsorption of L-cysteine, the growth rate of the crystal surface was reduced while the growths of other planes were promoted. Along with the formation of two-dimensional nanosheet of $BiVO_4$, the carbon atoms were inserted into the $BiVO_4$ crystal lattice. Under the effect of PVP, the generated two-dimensional particles were selectively assembled into a 3D flower-like C-doped $BiVO_4$.

According to the mechanism of degradation in Fig. 13, upon visible-light excitation, the P-L-$BiVO_4$ surface generates electron–hole pairs. Then, the photogenerated electrons react with dissolved oxygen molecules (O_2) to yield superoxide radical anions ($\cdot O_2^-$). The holes can react with OH^- to form ·OH, and through a series of reactions with H_2O, the activated $\cdot O_2^-$ further forms ·OH and O_2. The holes, $\cdot O_2^-$, and ·OH are strong oxidizing agents for the decomposition of organic dyes (Du et al. 2016). The entire sequence is summarized as follows:

$$\text{P-L-BiVO}_4 + h\nu\,(\text{visible light}) \rightarrow h^+ + e^- \quad \text{R1}$$
$$O_2 + e^- \rightarrow \bullet O_2^- \quad \text{R2}$$
$$\bullet O_2^- + H_2O \rightarrow \bullet OH + OH^- + O_2 \quad \text{R3}$$
$$h^+ + OH^- \rightarrow \bullet OH \quad \text{R4}$$
$$h^+ \text{or} \bullet O_2^- \text{or} \bullet OH + \text{RhB} \rightarrow \text{degraded products} \quad \text{R5}$$

Stability evaluation through recycling test

The stability of P-L-$BiVO_4$ is a major factor affecting its application effect. The stability of P-L-$BiVO_4$ was investigated through cyclic degradation of RhB under visible-light irradiation, as shown in Fig. 14a. The results show that the degradation rate of RhB tends to be nearly constant over five cycles. In the repeated tests, the degradation rate after each cycle is maintained at 73.24, 73.05, 72.45, 71.58, and 70.41%, respectively. The P-L-$BiVO_4$ sample was easily recycled by simple filtration. In addition, the phase structures of the sample remain unchanged, which verifies that the components of the P-L-$BiVO_4$ are difficult to be photodecomposed and its structure is stable during the photocatalytic process. This feature is very important for its practical application and modification.

Conclusions

In this paper, carbon-doped nanosheets m-$BiVO_4$ with 3D hierarchical structure and high visible-light photocatalytic property was synthesized by one-step hydrothermal method. The as-synthesized samples were characterized using various analytical methods, and their morphologies and compositions were thoroughly investigated as well. L-Cysteine was used as the carbon source for C-doping and the simultaneous control of the crystal morphology of $BiVO_4$. The photocatalytic activities of resulted samples were estimated by testing the photodegradation degree of RhB under visible-light irradiation. The results showed that the carbon-doped nanosheets $BiVO_4$ in 3D hierarchical structure had a significantly higher photocatalytic activity as compared to the $BiVO_4$ in sheet or amorphous form. In addition, C-doped 3D hierarchical nanosheets $BiVO_4$ with high visible-light photocatalytic property can easily be recycled without decreasing the photocatalytic activity. This new material is expected to be applied in future applications.

Acknowledgements Financial support from the Science and Technology Innovation Special Projects of Social Undertakings and Livelihood Support, Chongqing (cstc2016shmszx20009), the Science and Technology Project of Chongqing Education Commission (KJ1500604), the Graduate Scientific Research and Innovation Foundation of Chongqing, China (CYB16008), the Chongqing Research Program of Basic Research and Frontier Technology (cstc2015jcyjA20013), and the 111 Project (B13041) are gratefully acknowledged.

Compliance with ethical standards

Funding This study was funded by the Science and Technology Innovation Special Projects of Social Undertakings and Livelihood Support, Chongqing (cstc2016shmszx20009), the Science and Technology Project of Chongqing Education Commission (KJ1500604), the Graduate Scientific Research and Innovation Foundation of Chongqing, China (CYB16008), the Chongqing Research Program of Basic Research and Frontier Technology (cstc2015jcyjA20013), and the 111 Project (B13041).

Conflict of interest X.X. has received research grants from the Science and Technology Innovation Special Projects of Social Undertakings and Livelihood Support, Chongqing (cstc2016shmszx20009), and the 111 Project (B13041). D.Z. has received research grants from the Graduate Scientific Research and Innovation Foundation of Chongqing, China (CYB16008). Z.F. has received research grants from the Science and Technology Project of Chongqing Education Commission (KJ1500604) and the Chongqing Research Program of Basic Research and Frontier Technology (cstc2015jcyjA20013). W.Z., Y.-W.F., S.X., M.D., T.W., and F.J. declare that they have no conflicts of interest.

References

Allured B, Delacruz S, Darling T, Huda MN, Subramanian V (2014) Enhancing the visible light absorbance of $Bi_2Ti_2O_7$ through Fe-substitution and its effects on photocatalytic hydrogen evolution. Appl Catal, B 144:261–268

Azman NZN, Musa NFL, Razak NNANA, Ramli RM, Mustafa IS, Rahman AA, Yahaya NZ (2016) Effect of Bi_2O_3 particle sizes and addition of starch into Bi_2O_3–PVA composites for x-ray shielding. Appl Phys A Mater Sci Process 122:818

Bellaiche L, Vanderbilt D (2000) Virtual crystal approximation revisited: application to dielectric and piezoelectric properties of perovskites. Phys Rev B 61:7877

Blöchl PE (1994) Projector augmented-wave method. Phys Rev B 50:17953

Chang C, Teng F, Liu Z (2016) Fully understanding the photochemical properties of $Bi_2O_2(CO_3)1–xSx$ nanosheets. Langmuir 32:3811–3819

Cui WB, Liu W, Zhang Q, Li B, Liu XH, Yang F, Zhao XG, Zhang ZD (2010) Carbon-doping effects on the metamagnetic transition and magnetocaloric effect in MnAsC x. Journal of Magnetism & Magnetic Materials 322:2223–2226

Du M, Xiong S, Wu T, Zhao D, Zhang Q, Fan Z, Zeng Y, Ji F, He Q, Xu X (2016) Preparation of a microspherical silver-reduced graphene oxide-bismuth vanadate composite and evaluation of its photocatalytic activity. Materials 9:160

Galembeck A, Alves OL (2000) $BiVO_4$ thin film preparation by metalorganic decomposition. Thin Solid Films 365:90–93

Geng Y, Zhang P, Kuang S (2014) Fabrication and enhanced visible-light photocatalytic activities of $BiVO_4/Bi_2WO_6$ composites. RSC Adv 4:46054–46059

Gong Q, Qian X, Ma X, Zhu Z (2006) Large-scale fabrication of novel hierarchical 3D $CaMoO_4$ and $SrMoO_4$ mesocrystals via a microemulsion-mediated route. Cryst Growth Des 6:1821–1825

Grassmann O, Löbmann P (2003) Morphogenetic control of calcite crystal growth in sulfonic acid based hydrogels. Chemistry 9:1310–1316

Hu L, Dong S, Li Q, Feng J, Pi Y, Liu M, Sun J, Sun J (2015) Facile synthesis of $BiOF/Bi_2O_3$/reduced graphene oxide photocatalyst with highly efficient and stable natural sunlight photocatalytic performance. J Alloys Compd 633:256–264

Huang Y, Zhou L, Yang L, Tang Z (2011) Self-assembled 3D flower-like $NaY(MoO_4)_2:Eu^{3+}$ microarchitectures: hydrothermal synthesis, formation mechanism and luminescence properties. Opt Mater 33:777–782

Huang H, Liu L, Zhang Y, Tian N (2015) Novel $BiIO_4/BiVO_4$composite photocatalyst with highly improved visible-light-induced photocatalytic performance for rhodamine B degradation and photocurrent generation. RSC Adv 5:1161–1167

Iwase A, Kudo A (2010) Photoelectrochemical water splitting using visible-light-responsive $BiVO_4$ fine particles prepared in an aqueous acetic acid solution. J Mater Chem 20:7536–7542

Jagadale TC, Takale SP, Sonawane RS (2008) N-doped TiO_2 nanoparticle based visible light photocatalyst by modified peroxide sol−gel method. J Phys Chem C 112:14595–14602

Kho YK, Teoh WY, Iwase A, Mädler L, Kudo A, Amal R (2011) Flame preparation of visible-light-responsive $BiVO_4$ oxygen evolution photocatalysts with subsequent activation via aqueous route. ACS Appl Mater Interfaces 3:1997–2004

Kudo A, Ueda K, Kato H, Mikami I (1998) Photocatalytic O_2 evolution under visible light irradiation on $BiVO_4$ in aqueous $AgNO_3$ solution. Catal Lett 53:229–230

Kudo A, Omori K, Kato H (1999) A novel aqueous process for preparation of crystal form-controlled and highly crystalline $BiVO_4$ powder from layered vanadates at room temperature and its photocatalytic and photophysical properties. J Am Chem Soc 121:11459–11467

Kvítek L, Panáček A, Soukupová J, Kolář M, Večeřová R, Prucek R, Holecová M, Zbořil R (2008) Effect of surfactants and polymers on stability and antibacterial activity of silver nanoparticles (NPs). J Phys Chem C 112:5825–5834

Li J-Q, Guo Z-Y, Liu H, Du J, Zhu Z-F (2013) Two-step hydrothermal process for synthesis of F-doped $BiVO_4$ spheres with enhanced photocatalytic activity. J Alloys Compd 581:40–45

Li H, Sun Y, Cai B, Gan S, Han D, Niu L, Wu T (2015) Hierarchically Z-scheme photocatalyst of Ag@AgCl decorated on $BiVO_4$ (040) with enhancing photoelectrochemical and photocatalytic performance. Appl Catal B Environ 170-171:206–214

Lim AR, Choh SH, Jang MS (1998) Prominent ferroelastic domain walls in $BiVO_4$ crystal. J Phys Condens Matter 7:7309–7323

Liu JB, Wang H, Wang S, Yan H (2003) Hydrothermal preparation of $BiVO_4$ powders. Mater Sci Eng B 104:36–39

Liu W, Cao L, Su G, Liu H, Wang X, Zhang L (2010) Ultrasound assisted synthesis of monoclinic structured spindle $BiVO_4$ particles with hollow structure and its photocatalytic property. Ultrason Sonochem 17:669–674

Manna G, Bose R, Pradhan N (2014) Photocatalytic Au–Bi_2S_3 heteronanostructures. Angew Chem Int Ed 53:6861–6864

Natarajan TS, Bajaj HC, Tayade RJ (2014) Synthesis of homogeneous sphere-like Bi_2WO_6 nanostructure by silica protected calcination with high visible-light-driven photocatalytic activity under direct sunlight. CrystEngComm 17:1037–1049

Natarajan K, Bajaj HC, Tayade RJ (2016) Photocatalytic efficiency of bismuth oxyhalide (Br, Cl and I) nanoplates for RhB dye degradation under LED irradiation. J Ind Eng Chem 34:146–156

Payne D, Robinson M, Egdell R, Walsh A, McNulty J, Smith K, Piper L (2011) The nature of electron lone pairs in $BiVO_4$. Appl Phys Lett 98:212110

Strobel R, Metz HJ, Pratsinis SE (2008) Brilliant yellow, transparent pure, and SiO_2-coated $BiVO_4$ nanoparticles made in flames. Chem Mater 20:6346–6351

Su J, Guo L, Yoriya S, Grimes CA (2009) Aqueous growth of pyramidal-shaped $BiVO_4$ nanowire arrays and structural characterization: application to photoelectrochemical water splitting. Cryst Growth Des 10:856–861

Sun, Y., Wu, C., Long, R., Cui, Y., Zhang, S., Xie, Y. (2009) Synthetic loosely packed monoclinic $BiVO_4$ nanoellipsoids with novel multiresponses to visible light, trace gas and temperature. Chem Commun (Camb): 4542–4544

Tang D, Zhang H, Huang H, Liu R, Han Y, Liu Y, Tong C, Kang Z (2013) Carbon quantum dots enhance the photocatalytic performance of $BiVO_4$ with different exposed facets. Dalton Trans 42:6285–6289

Uddin I, Ahmad A, Siddiqui EA, Hasanur RS, Gambhir S (2016) Biosynthesis of fluorescent Bi_2S_3 nanoparticles and their application as dual-function SPECT-CT probe for animal imaging. Curr Top Med Chem 16:2019

Wang T, Markus A, Helmut C (2006) Calcite mesocrystals: "morphing" crystals by a polyelectrolyte. Chem Eur J 12: 5722–5730

Wang Z, Luo W, Yan S, Feng J, Zhao Z, Zhu Y, Li Z, Zou Z (2011) $BiVO_4$ nano-leaves: mild synthesis and improved photocatalytic activity for O_2 production under visible light irradiation. CrystEngComm 13:2500

Wang M, Niu C, Liu Q, Che Y, Liu J (2014a) Enhanced photodegradation methyl orange by N–F co-doped $BiVO_4$ synthesized by sol–gel method. Mater Sci Semicond Process 25: 271–278

Wang Y, Zhao J, Zhou B, Zhao X, Wang Z, Zhu Y (2014b) Three-dimensional hierarchical flowerlike microstructures of α-Bi_2O_3 constructed of decahedrons and rods. J Alloys Compd 592:296–300

Wei L, Yu Y, Cao L, Ge S, Liu X, Lan Z, Wang Y (2010) Synthesis of monoclinic structured $BiVO_4$ spindly microtubes in deep eutectic solvent and their application for dye degradation. J Hazard Mater 181:1102–1108

XHG, Yu SH (2007) Controlled mineralization of barium carbonate mesocrystals in a mixed solvent and at the air/solution interface using a double hydrophilic block copolymer as a crystal modifier. Cryst Growth Des 7:354–359

Xi G, Ye J (2010) Synthesis of bismuth vanadate nanoplates with exposed {001} facets and enhanced visible-light photocatalytic properties. Chem Commun (Camb) 46:1893–1895

Xie B, Zhang H, Cai P, Qiu R, Xiong Y (2006) Simultaneous photocatalytic reduction of Cr(VI) and oxidation of phenol over monoclinic $BiVO_4$ under visible light irradiation. Chemosphere 63:956–963

Xie D, Su Q, Dong Z, Zhang J, Du G (2013) L-Cysteine-assisted preparation of porous NiO hollow microspheres with enhanced performance for lithium storage. CrystEngComm 15: 8314–8319

Xiong T, Dong F, Wu Z (2014) Enhanced extrinsic absorption promotes the visible light photocatalytic activity of wide band-gap $(BiO)_2CO_3$ hierarchical structure. RSC Adv 4: 56307–56312

Xu AW, Antonietti M, Cölfen H, Fang YP (2006) Uniform hexagonal plates of vaterite $CaCO_3$ mesocrystals formed by biomimetic mineralization. Adv Funct Mater 16:903–908

Xu H, Li H, Wu C, Chu J, Yan Y, Shu H, Gu Z (2008) Preparation, characterization and photocatalytic properties of Cu-loaded $BiVO_4$. J Hazard Mater 153:877–884

Yan Y, Zhou Z, Cheng Y, Qiu L, Gao C, Zhou J (2014) Template-free fabrication of α- and β-Bi_2O_3 hollow spheres and their visible light photocatalytic activity for water purification. J Alloys Compd 605:102–108

Yin C, Zhu S, Chen Z, Zhang W, Gu J, Zhang D (2013) One step fabrication of C-doped $BiVO_4$ with hierarchical structures for a high-performance photocatalyst under visible light irradiation. J Mater Chem A1:8367

Yu SH, Golfen H (2004) Bio-inspired crystal morphogenesis by hydrophilic polymers. J Mater Chem 14:2124–2147

Yu J, Zhang Y, Kudo A (2009) Synthesis and photocatalytic performances of $BiVO_4$ by ammonia co-precipitation process. J Solid State Chem 182:223–228

Zhang A, Zhang J (2010) Synthesis and characterization of Ag/$BiVO_4$ composite photocatalyst. Appl Surf Sci 256:3224–3227

Zhang L, Chen D, Jiao X (2006) Monoclinic structured $BiVO_4$ nanosheets: hydrothermal preparation, formation mechanism, and coloristic and photocatalytic properties. J Phys Chem B 110:2668–2673

Zhang HM, Liu JB, Wang H, Zhang WX, Yan H (2008a) Rapid microwave-assisted synthesis of phase controlled $BiVO_4$ nanocrystals and research on photocatalytic properties under visible light irradiation. J Nanopart Res 10:767–774

Zhang X, Ai Z, Falong Jia A, Zhang L (2008b) Generalized one-pot synthesis, characterization, and photocatalytic activity of hierarchical BiOX (X = Cl, Br, I) nanoplate microspheres. J Phys Chem C 112:747–753

Zhang A, Zhang J, Cui N, Tie X, An Y, Li L (2009a) Effects of pH on hydrothermal synthesis and characterization of visible-light-driven $BiVO_4$ photocatalyst. J Mol Catal A Chem 304:28–32

Zhang X, Chen S, Quan X, Zhao H (2009b) Preparation and characterization of $BiVO_4$ film electrode and investigation of its photoelectrocatalytic (PEC) ability under visible light. Sep Purif Technol 64:309–313

Zhang LS, Wong KH, Yip HY, Hu C, Yu JC, Chan CY, Wong PK (2010) Effective photocatalytic disinfection of *E. coli* K-12 using AgBr-Ag-Bi_2WO_6 nanojunction system irradiated by visible light: the role of diffusing hydroxyl radicals. Environ Sci Technol 44:1392–1398

Zhao Z, Dai H, Deng J, Liu Y, Au CT (2013) Effect of sulfur doping on the photocatalytic performance of $BiVO_4$ under visible light illumination. Chin J Catal 34:1617–1626

Zhao D, Zong W, Fan Z, Xiong S, Du M, Wu T, Fang Y-W, Ji F (2016) Synthesis of carbon doped $BiVO_4$@multi-walled carbon nanotubes with high visible light absorption behavior and evaluation of its photocatalytic property. CrystEngComm 18: 9007–9015